RESEARCH PAPER

Site monitor based on the RINGSS concept

Edison Bustos,* Andrei Tokovinino,* and Rossano Rivera Cerro Tololo Inter-American Observatory - NSFs NOIRlab, La Seerena, Chile

ABSTRACT. We provide a detailed description of the turbulence profiler based on the RINGSS concept (analysis of scintillation in a small telescope). The instrument uses the 5-in. Celestron telescope and the low-noise CMOS cameras ASI290MM or ASI462MM. Coupled with a compact harmonic-drive mount, it fits in a small enclosure, thereby reducing both the cost and the wind buffeting. Two concepts of custom compact enclosures are presented. The software used for data acquisition, processing, and robotic control is written in Python and is available online; its algorithms are outlined. As application examples, we provide a comparison between RINGSS and the regular MASS-DIMM site monitor at Cerro Tololo, a summary of the 2023 Paranal campaign, and a characterization of an alternative site using a portable instrument. Overall, RINGSS appears to be an affordable and robust solution for site monitoring.

© 2025 Society of Photo-Optical Instrumentation Engineers (SPIE) [DOI: 10.1117/1.JATIS.11.2.027001]

Keywords: site testing; turbulence profiler

Paper 25048G received Feb. 13, 2025; revised Apr. 29, 2025; accepted May 9, 2025; published Jun. 4, 2025.

1 Introduction

Astronomical observations from the ground and telecommunications are seriously affected by light propagation through optically inhomogeneous air; this phenomenon is generally referred to as optical turbulence. The perturbations are described by the vertical profile of the refractive index structure constant $C_n^2(h)$ (optical turbulence profile, OTP) and the related parameters such as seeing. These parameters and the underlying theory are covered in textbooks^{1,2} and reviews.^{3–5} Operation of modern telescopes (especially with adaptive optics) and characterization of new sites require monitoring of the OTP. There are various techniques for OTP measurement, for example, SCIDAR^{6,7} or Single-Star SCIDAR.^{8,9} This paper describes one particular instrument based on the analysis of single-star scintillation.

A practical and inexpensive way to measure low-resolution OTPs and seeing is offered by a combination of the differential image motion monitor, DIMM, ^{10,11} with a Multi-Aperture Scintillation Sensor, MASS, 12 that uses the scintillation of single bright stars to probe the turbulence. Such instruments are currently installed at several observatories and have also served for the characterization of new sites. 13 However, MASS employs an obsolete technology (photo-multipliers). Its replacement, the Ring-Image Next Generation Scintillation Sensor (RINGSS), is based on a low-noise CMOS detector. The principle of RINGSS, the underlying theory, and the first tests are covered in Ref. 14. Here, we provide a detailed description of a particular implementation of this idea, focusing on the technical aspects and software. This paper is timely because such instruments rapidly gain popularity.

A turbulence profiler must operate robotically on clear nights and deliver data in real time. Owing to the approximate and nonstationary nature of the OTP, the results must be given in

^{*}Address all correspondence to Edison Bustos, edison.bustos@noirlab.edu; Andrei Tokovinin, andrei.tokovinin@noirlab

absolute units without the need for external calibration; the accuracy, however, is intrinsically limited because all measured parameters are model-dependent, whereas the model is only a first-order approximation to the reality. Robustness of the operation and resilience to environmental factors such as wind, dust, and precipitation are important practical considerations for site monitors. The cost of constructing a site monitoring and maintaining its operation is another relevant factor. We show how the RINGSS instrument matches these requirements and what potential improvements can be made.

2 Operational Principles and Overview

The RINGSS turbulence monitor is based on recording a series of defocused short-exposure images of a single bright star in a small telescope with an annular aperture. ¹⁴ The optics forms ring-like images, focused in the radial direction. Scintillation (twinkling) of the star produces fluctuations of the flux at the telescope aperture and along the ring (in azimuth), as shown in Fig. 1. The characteristic size of these fluctuations depends on the propagation distance z and wavelength λ as $\sqrt{\lambda z}$: close-by distortions correspond to a low-contrast and small-scale pattern, whereas distant distortions produce a flux modulation of larger amplitude and size. Statistical analysis of the recorded ring images, analogous to a Fourier spectrum in the angular coordinate, is related to the OTP using the propagation theory and the instrument parameters. The same idea is implemented in MASS and some other single-star turbulence profilers. ^{15–18}

Technical implementations of the RINGSS idea can vary, depending on the requirements, selected hardware, etc.; one particular implementation is described in this paper. Figure 2



Fig. 1 Series of the ring images of the star HR 8728 recorded on October 6, 2023, at 0:13:36 UT. The first four consecutive instantaneous images and the average image are shown in negative rendering. The ring radius is 11.3 pixels.

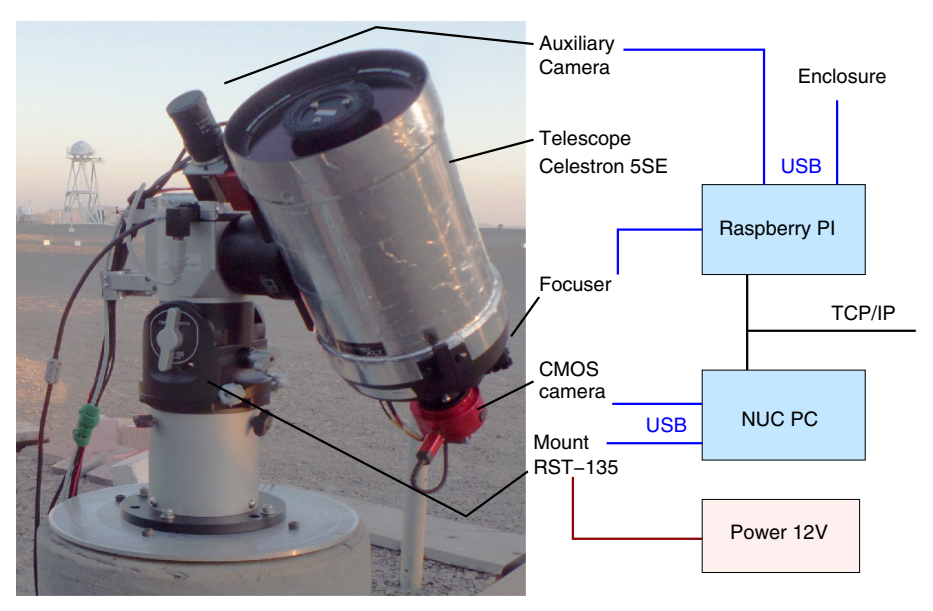


Fig. 2 Main components of the RINGSS turbulence monitor. The instrument is very compact (the outer diameter of the tube is 150 mm). The filters and lenses are housed in a small barrel between the camera and the telescope.

presents the main components of the RINGSS OTP monitor. In the picture taken at Paranal, the mount is configured in the alt-az mode and attached to a pillar by a small tube, without enclosure. All signal connections use the USB3 interface. The control is usually split between the Intel NUC computer (CMOS camera and mount, focus control, signal processing) and Raspberry PI (dome control and auxiliary camera), although a single computer can handle all tasks.

3 Optics and Detector

3.1 Optics

For practical reasons, it is preferable to build an OTP monitor using a small-aperture telescope. On the other hand, the number of collected stellar photons and the amplitude of atmospheric phase distortions increase with the aperture diameter D. Seeing monitors of previous generations typically had $D \sim 0.25$ m, but in RINGSS, D as small as ~ 0.1 m is feasible. We selected the commercial amateur Schmidt–Cassegrain telescope Celestron Nexstar 5SE (hereafter Celestron) for its compactness (tube length 270 mm, tube diameter 150 mm, mass 2.35 kg), good optical quality, and low cost. The meniscus securely protects all other optics from dust and water. The aperture diameter is 127 mm, and its outer annulus is not obstructed by spiders. The central obstruction is artificially increased from 0.39 to 0.5 by placing a circular mask of 63 mm diameter atop the meniscus.

The optical prescriptions of the Celestron telescopes are a commercial secret of the vendor. The starting point of the present design is an equivalent Richey-Chretien two-mirror reflector that matches the actual telescope approximately. Its prescription, listed in Table 1, is based on the optical parameters (F/10 beam) and dimensions (distance between the mirrors). The conic constant (CC) of the concave secondary mirror is -3.0, and the CC of the primary mirror is adjusted to -1.1382 to get a stigmatic on-axis image.

The ring image is produced by a conic wavefront. A good approximation of the cone is obtained by a combination of defocus and spherical aberration in suitable proportion, namely, $a_{11} \approx -0.1a_4$ (here, we use Noll's notation for Zernike aberrations). A positive achromatic lens L2 in front of the focus reduces the effective focal length, providing the optimum match to the small detector pixels, and at the same time gives the spherical aberration of correct sign for the intra-focal images (positive a_4 and negative a_{11}), so the right balance can be achieved at a certain value of the defocus. The residual chromatism of L2 is compensated by a negative singlet lens L1. Our optical design illustrated in Fig. 3 uses commercial lenses from Edmund Optics: the achromatic doublet #32-309 (diameter 12.5 mm, F = 20 mm) and the negative bi-convex lens #32-995 (diameter 25 mm, F = -100 mm). Their alternative part numbers in the table correspond to the same lenses with a VIS -0 deg coating.

The adjustable parameter of this design is the distance between the last lens and the camera, which we call l. With increasing l, the de-magnification factor k becomes larger, the beam footprint on the lens increases, and the residual spherical aberration a_{11} also increases. With l=13.5 mm, the effective focal length is 423 mm, and the pixel scale is 1.41'' for detector pixels of $2.9~\mu$ m. A conic wavefront is reached by moving the camera + lenses assembly forward by 3 mm, which corresponds to the image plane conjugation at 520 m below the ground. The resulting ring image shown in Fig. 3 has a geometric radius of $30.9~\mu$ m, or ~ 11 pixels.

Table 1 Optical parameters.

Element	Parameters	Dist. next	Comment
Primary M1	R = 435, CC = −1.1382	-163	Moves to adjust focus
Secondary M2	R = -132, CC = -3.0	163 + 120	Fixed
Negative lens L1	F = -100, D = 25	~12	EO #32-995, #47-919
Achromat L2	F = 20, D = 12.5	13.5*	EO #32-309, #47-661
Camera	Pixel 2.9 μ m	0	Focal plane

^{*}Adjustable parameter.

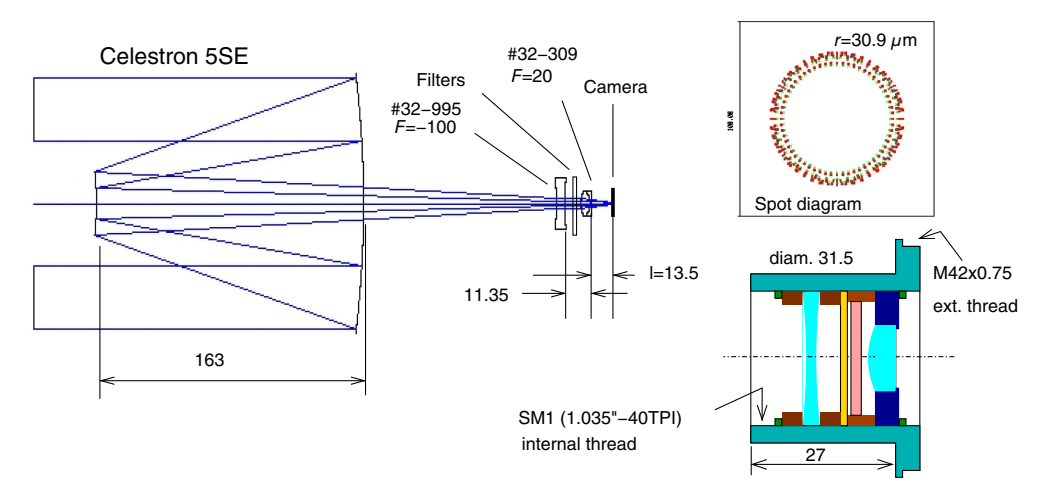


Fig. 3 Optical layout of RINGSS and spot diagram. The blue, red, and green colors in the spot diagram denote wavelengths of 0.5, 0.6, and 0.7 μ m, respectively. The sketch shows the barrel holding the lenses and filters (dimensions in millimeters).

The distance l is a very sensitive parameter. By moving the lenses further away from the camera by 0.5 mm (to l=14 mm), we would reduce the effective focal length to 407 mm. The spherical aberration increases, and a conic wavefront is obtained for a 4-mm defocus, where the ring radius increases to 41.2 μ m. On the other hand, the beam between L1 and L2 is almost parallel, and the spectral filters can be placed either between the lenses or in front of L1. The lenses and filters are assembled in a small barrel with an external diameter of 31.5 mm, inserted in place of the telescope eyepiece; the camera is connected to the barrel by the $M42 \times 0.75$ thread. The barrel allows for a small adjustment of the critical distance l.

3.2 Collimation and Focusing

Deviations of the wavefront from its nominal conic shape affect the response of RINGSS and, consequently, the results. Therefore, good-quality and stable optics are needed. The thermal change of focus is inevitable (the telescope tube is made of aluminum), so we implemented an active focus control. Fortunately, Celestron has a good internal focusing mechanism: rotation of the knob moves the primary mirror axially in a smooth way without tilts or hysteresis (unlike in some other cheap telescopes). We attached a servomotor AX-12A from Dynamixel to the focus knob of the Celestron. It is controlled digitally via an RS485-USB converter and powered by a 12v DC supply. The 1024 digital steps correspond to a motor shaft rotation of 300 deg, sufficient for our purpose (the ring radius increases by 1 pixel when the motor is moved by -14 steps). The control algorithm maintains a constant ring radius by adjusting the focus.

To eliminate the coma aberration, the telescope is collimated in the standard way, by tilting the secondary mirror. The collimation depends on the orientation of the barrel containing the lenses owing to their residual de-centering, so the clocking angle of the lenses and the detector is fixed by a pin to enable removal and insertion of the barrel at the same clocking angle.

The average ring image (see Fig. 1, right) contains information on low-order aberrations such as defocus, astigmatism, coma, and trefoil. This information is retrieved during data processing and kept in the output files; the coma amplitude and angle are also displayed in real time, helping us to collimate the optics. We found that the Celestron's alignment is stable in time, and there is no need to repeat it. If, for some reason, the optics have measurable aberrations, their influence can be accounted for in the calculation of the response, so the affected data can be reprocessed and corrected later. This option is implemented in the software, but, so far, it has never been used.

3.3 Auxiliary Camera

The auxiliary camera is used only during the initial setup, not in normal operation. It is the SVPRO 1800P USB camera model equipped with a zoom lens of 5 to 50 mm focal length. We adjust the zoom to cover a field of \sim 5 deg. We added a cross with a circle to the

camera-viewer software to mark the position of the telescope field center. Considering the large field, no mechanical adjustment of the camera is needed (it is fixed rigidly to the telescope's dovetail rail), whereas the cross position is tuned in the software. Stars as faint as the sixth magnitude are seen in the live display of this camera.

3.4 CMOS Camera

The light detector is a critical element of the RINGSS instrument. We selected the inexpensive scientific CMOS monochrome camera ASI290MM from ZWO.¹⁹ This product was developed primarily for astro-photography. The pixel size is $2.9 \, \mu m$, format 1936×1096 pixels (size 5.6×3.2 mm), readout noise (RON) ~1 el., and maximum quantum efficiency 0.80. The detector is a back-illuminated CMOS chip IMX290 from Sony. It is not cooled, but at short exposures, the dark current is negligibly small. The camera body has a diameter of 62 mm and weights 120 g. It allows a frame rate of 737.5 frames per second (FPS) for a region of interest (ROI) of 320×240 pixels. This camera is now replaced by ASI462MM, which has the same detector geometry, a lower RON, and a larger sensitivity in the red.²⁰ Both cameras are connected to the computer and powered by the USB3.0 interface. The signal depth is 12 bit.

We studied this camera in the laboratory and confirmed its excellent characteristics given by the vendor. In the acquisition software, the 16-bit raw signal received from the camera is divided by 16 to match its true 12-bit depth (the saturation value is thus 4095 rather than 65,535 ADU). The conversion factor g from ADU to electrons depends on the internal gain G specified in units of 0.1 dB (a change by 200 units corresponds to a 10× change of g). The conversion factor is thus expressed by the equation

$$g = C \, 10^{-G/200},\tag{1}$$

where the constant C equals 3.6 el/ADU for ASI290MM and 2.8 el/ADU for ASI462MM. The gain factors reported by the camera are found in the comments section of the image headers recorded by our software. We operate RINGSS with G=200. The mean RON at this gain is 1.19 el. for ASI290MM and 0.8 el. for ASI462MM. The fraction of fixed pixels where the RON exceeds its mean value by a factor of 3 or more is \sim 0.2%. The presence of noisy pixels with an increased RON is typical for other high-end CMOS cameras. In the case of RINGSS, the photon noise dominates, so the exact value of RON is not critical. The sensitivity is very uniform over the field, with an rms variation of 0.8%. In a small (0.1%) fraction of pixels, the sensitivity exceeds its mean value by 3% or more. There are also some "hot" pixels with increased dark current.

In RINGSS, a small ROI of 64×64 or 48×48 pixels is selected, and a series of 2000 consecutive images with a 1 ms exposure (a data cube) are recorded. We checked the uniformity of the temporal sampling by recording cubes with a light source pulsating at 100 Hz (a neon lamp). The frame rate of the data cubes captured by our system with 1 ms exposure is 994 FPS. Other image acquisition tools, e.g., ASICAP provided by the camera vendor, suffer from occasional missing or duplicated images.

3.5 Spectral Response

Conversion of the measurements into a turbulence profile depends on the spectral response of the instrument and the spectrum of the light source (star). To reduce this dependence, the spectral bandwidth must be restricted by filters. We selected the short-pass interference filter FE0750 in combination with the long-pass yellow glass filter FG455 from Thorlabs. Figure 4 plots the product of the filter transmission and the detector quantum efficiency specified by the vendor. This choice is a compromise between collecting a larger number of stellar photons and reducing the impact of the stellar spectrum on the results.

The actual response of the instrument has been checked by observing several bright stars with B-V colors ranging from -0.4 (blue) to 1.5 (red) and recording their fluxes. The expected magnitudes in the instrumental system M and in the standard B and V bands were computed for black body spectra with temperatures from 3000 to 10,000 K, and the theoretical dependence of M-V on the B-V color was established and compared with the actual data. The first test with just the FE0750 filter has shown a disagreement, revealing that this filter has a larger blue leak than specified by the vendor. Therefore, the blocking yellow filter is indeed necessary. With this

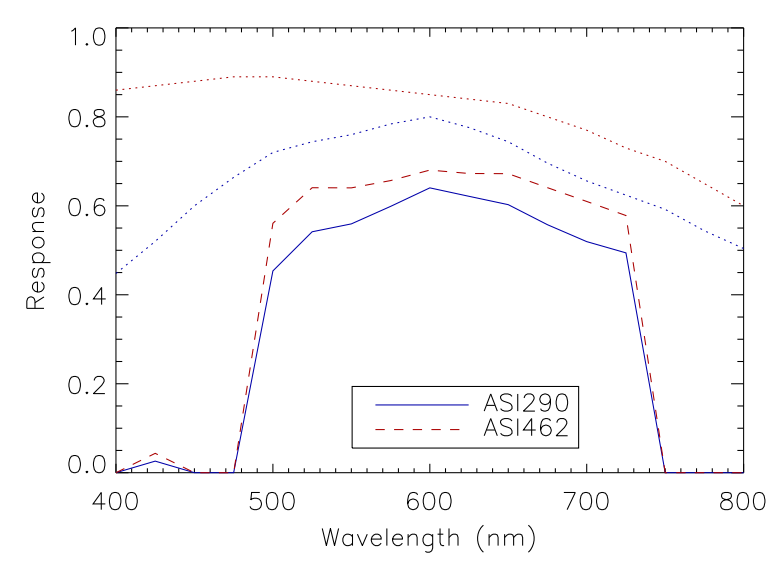


Fig. 4 Quantum efficiency of the CMOS cameras ASI290MM and ASI462MM (dotted lines) and their product by the transmission curves of the Thorlabs filters FE0750 and FG455 (dash).

filter, we fitted a linear regression $M - V \approx 0.40 - 0.33(B - V)$ to the data; its slope matches the expected one, -0.33, thus verifying the spectral response.

4 Mount and Enclosure

4.1 Mount

We selected a compact and robust harmonic-drive mount RST-135 from Rainbow Astro. This relatively new technology provides a very high stiffness and does not require any balancing counterweights. The mount can be operated in either equatorial or alt-az modes. Importantly, it has internal zero-point sensors, allowing remote pointing recovery (e.g., after a power cut). The mount is controlled by the computer via a USB line, and a hand paddle for manual control is also available. The mount software provides an internal pointing model to correct residual setup errors, and this model is used in RINGSS. A blind pointing accuracy of better than 1' is achieved after acquiring and centering 4 to 5 stars, so the auxiliary camera is no longer needed after establishing the pointing model. During tracking, the star remains stationary in the field, but occasionally, it moves by ~20 " when the teeth of the harmonic drive are changed. This feature, common to all harmonic drive mounts, is not detrimental to the RINGSS operation.

We constructed our first RINGSS system using the mount in the equatorial mode. In this mode, the mount's internal algorithm places the tube on the eastern side when the pointed star has passed the meridian and on the western side otherwise, and the operator has no control over those meridian flips. Depending on the flip, the sense of the RA correction is inverted, and this is accounted for in our guiding software. In other RINGSS instruments, we configured the mount in the alt-az mode, as shown in Fig. 2. In the parked (home) position, the tube is on the western side of the mount, pointing North (in the southern hemisphere), AZ = EL = 0. The azimuth changes within ± 220 deg, depending on the star location, but the mount never makes larger azimuth excursions, so there is no risk of cables becoming wound around the vertical column. When the column is set up vertically, the initial azimuth of the mount is established by pointing to a bright star or a planet. Then, the pointing model is determined, taking care of the residual errors; there is no need for a mechanical polar alignment.

4.2 Cylindrical Enclosure

Our RINGSS project envisioned from the outset monitoring and observing conditions at remote sites. A transportable and robust enclosure protecting the instrument securely from precipitation and dust is an essential component of such a monitor. We could not find suitable commercial solutions for the enclosure and developed our own concept, illustrated in Fig. 5. The mount is

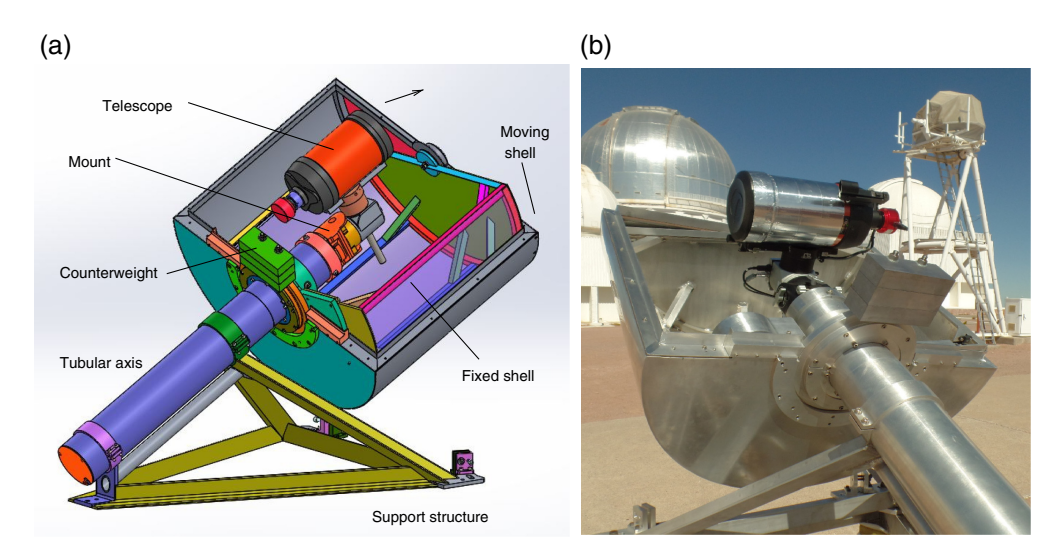


Fig. 5 Mechanical concept of the cylindrical enclosure (a) and its photograph (b) (in the opened state).

surrounded by a cylindrical enclosure concentric with the Polar axis. Both the mount and the cylinder are attached to a sturdy base tube, itself mounted on a pyramidal truss. All cables go through the base tube. The whole unit can be loaded on a pickup truck for transportation to remote sites.

The lower part of the cylinder, made of a 1.6-mm-thick aluminum sheet with reinforcing ribs, is fixed to the base tube. The movable upper half of the cylinder, of a slightly larger diameter, rotates, driven by the sector gear and the geared stepper motor located inside. The outer diameter of the moving shell is 723 mm, and the length of the cylinder is 634 mm. The enclosure provides a minimum clearance of 2 cm at all possible positions of the telescope. A counterweight balances the axial torque of the moving part. In the closed state, the halves of the cylinder connect via plastic elements, so that rain, snow, or dust cannot enter inside even under strong wind. In the case of a motor failure, the enclosure can be opened manually by disengaging the sector gear from the motor, acting from the outside. We specified the motor force sufficient for closing reliably against a strong wind of 25 m/s. The outer aluminum surface is polished to reduce the radiative cooling, and for the same reason, the telescope tube is covered by aluminum foil.

This enclosure has been mounted on the 6-m high tower and, together with the RINGSS instrument, has operated as a regular site monitor at Cerro Tololo since November 2022. The optics inside remain very clean. An unexpected test of resilience occurred in August 2024, when the enclosure was inadvertently left open during a strong snowstorm. It was completely inundated by the melted show. Yet, we could revive the enclosure itself and all other elements of the instrument, without any permanent damage.

4.3 Box-Type Enclosure

Fabrication of the cylindrical enclosure consumed substantial effort. Looking for cheaper and simpler options, we constructed an alternative box-type enclosure presented in Fig. 6; it is adapted for the alt-az mount. The volume swept by the telescope and mount is approximately a cylinder of 300 mm radius and 400 mm height. It fits inside a square box of 650 mm inner size. The box is covered by two petals that rotate by 90 deg, driven by two cheap linear actuators ECO LC6 (200-mm stroke) and levers. The actuators are designed for outdoor use.

Each petal is driven from one side, so some torsional stiffness of the petals is required. They are assembled from aluminum sheets and a 25-mm lightweight square profile that provides most of the stiffness. In the closed state, the petals are pressed against each other, and the torsional compliance acts as a restoring force, securing the closed gap; regulation of the actuator's position in the closed state achieves a uniform closure along the gap. Water is prevented from entering the gap by plastic seals glued atop the petals.

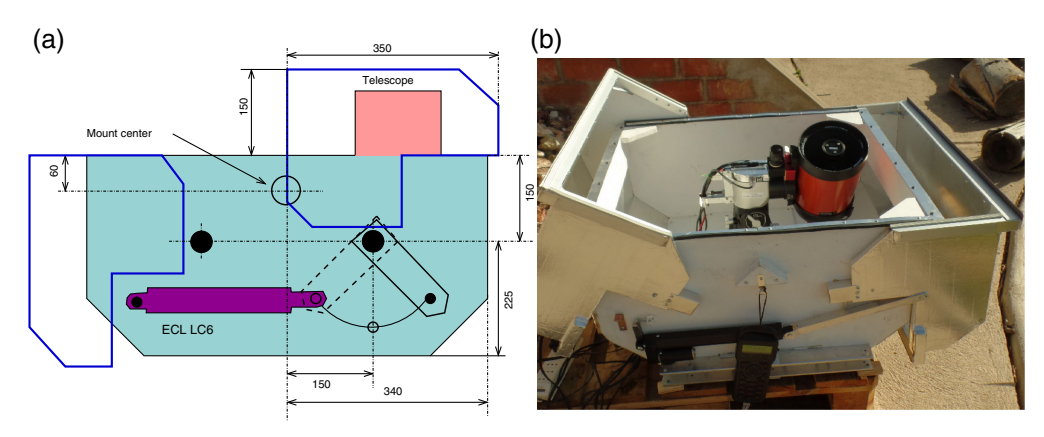


Fig. 6 Dimension of the box-type enclosure (a) (one petal opened and one closed) and its picture (b).

The box is constructed from 15-mm plywood around a rigid aluminum base. The base is attached to the tower and also holds the mount, providing its mechanical connection to the tower. In the opened state, the enclosure presents a low profile to the wind, thus reducing the buffeting.

The cables are assembled in a bundle on the mount side opposite to the telescope, descend on the box floor, and exit through a small hatch in the lower corner of the enclosure. The sufficient length of the cables allows rotation in azimuth by ± 220 deg around the nominal (parking) position.

This box-type enclosure has been installed on a 3-m tower near the SARA telescope at Cerro Tololo and worked for several months (Sec. 6.3). The two enclosure concepts outlined here are viable solutions, but alternative designs are certainly feasible. In principle, the mount and the telescope can be protected from the environment individually, eliminating the need for a separate enclosure.

5 Software

Although the hardware of the RINGSS turbulence monitor is almost standard (except the enclosures), its software is the most important "custom" part of the system. The algorithm for measuring turbulence parameters from ring-like images has been thoroughly described in Ref. 14. It has been developed in IDL. In 2021, the software was coded in Python 3.8 to make it openly accessible without an IDL license (The code is posted at Ref. 21 and at Zenodo https://doi.org/10.5281/zenodo.14865456). This Python version is described here with emphasis on the data organization, workflow, and instrument control. The following Python packages are used: numpy, scipy (optimize), astropy (io, time, units, coordinates), open-cv, and wxPython for GUIs. The vendor's camera library file and the zwoasi Python package are used for image acquisition and processing. The simulation tools are not yet ported from IDL to Python.

The acquisition software takes sequences of consecutive short-exposure (1 ms) images, i.e., the image cubes (typically 2000 frames of 64×64 or 48×48 pixels each). Originally, the cubes were recorded on the disk, but now, they are processed "on the fly" immediately after the acquisition. The results of processing each data cube are appended as a new line to the .stm (statistical moments) text file. This file, together with the system parameters, constitutes the input data for the calculation of the turbulence profile. The system parameters and other intermediate data are dictionaries stored in the JSON format, depicted by the pink boxes in Fig. 7. The code is organized so that each software module is given only the required data and ignores other data, thus separating the tasks and eliminating mutual dependencies as much as possible. The common instrument parameters are used by almost all modules.

A modular software architecture based on TCP/IP sockets (Fig. 7) is adopted. The TCP/IP socket communication protocol has been used in other turbulence profiling systems, e.g., in MASS-DIMM. The top-level program that orchestrates the operation, the *Director* (analog of the old supervisor program), connects by sockets to the individual software components that manage the camera, the mount, the focuser, the dome, etc. Each component is a socket server that receives commands and responds to the director's requests. The Director "knows" only the

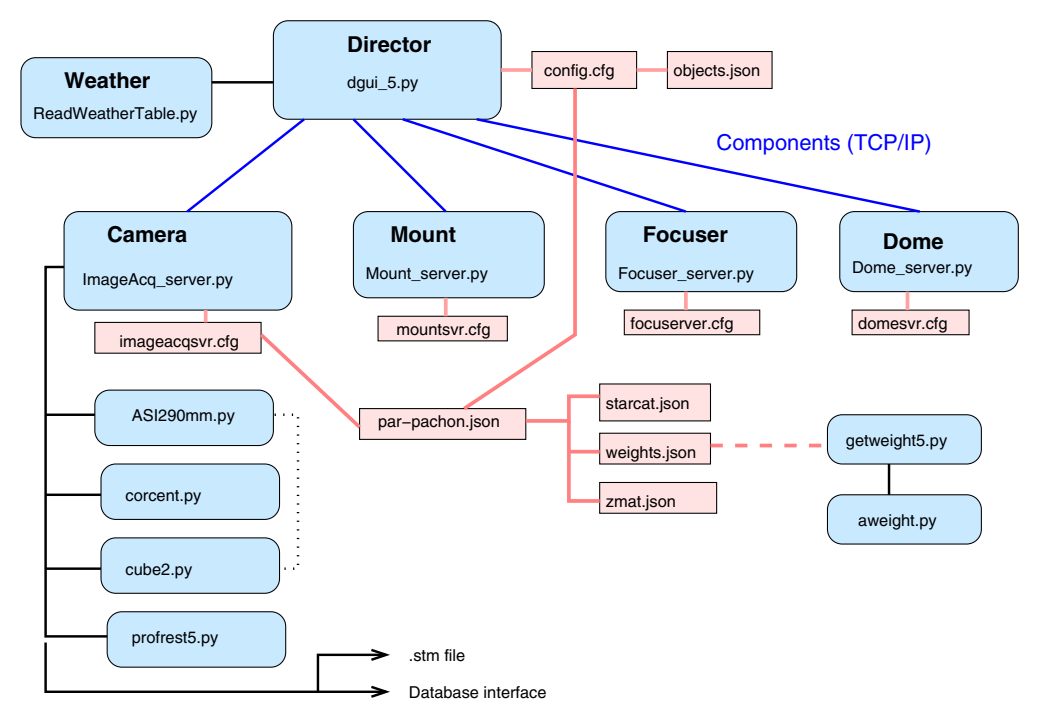


Fig. 7 Top-level diagram of the software components (blue boxes) and associated configuration files (pink).

essential information needed to organize the interaction between the components (pointing, centering, guiding, focusing). By far the most important component is a camera that actually performs acquisition and turbulence measurements. The Director is relatively independent of the underlying components. In normal operation, all components must be running; otherwise, the Director simply complains and stops the operation. The connection to the weather service is implemented as part of the Director, not as a separate component.

5.1 Configuration Files

The director's configuration file is an ASCII JSON file that defines the overall system. {
 "Site":{"Name":"PAC","Longitude":"-70.7358","Latitude":

```
"-30.2401",
"Elevation": "2709", "Horizon": "-7"
},
"Component": {
  "Mount": { "host": "localhost", "port": 16021},
  "Camera": { "host": "localhost", "port": 20402 },
  "Focuser": { "host": "localhost", "port": 26121},
  "Dome":"{host":"122.17.180.55", "port":29024}
},
"Object": "object_2025.json",
"Par": "../camera/par-pachon.json",
"General": { "auto": 1, "timer": 3, "wait_auto_mode": 30,
  "wait_if_clouds":30, "wait_if_bad_weather":3000,
  "hum_max":80.0,
  "wspd max":15.0, "mount mode": "altaz", "center thr":5,
  "guide_thr":3,
  "M00":0.7, "M01":0.0, "M10":0.0, "M11":0.7, "Cspeed":20,
  "Gspeed":1.0,
  "maxtime":5, "radius_thr":0.5,
  "focus_step_incr":15, "number_of_cubes":10}
```

The site section is required to calculate the sun's altitude. The component section is where the software components are defined by the hostname and the socket. The parameter object sets the file name where the star list is defined. *Par* is the instrument parameter file name (the same file must be used by the camera component). The general section is a set of global parameters required for robotic operation, such as minimum weather conditions for operation.

Each software component has its own parameter file that at least has the server definition where the socket is set. This socket must match the Director's configuration file.

The camera component configuration file is the most important. The Sitepar is the same file used by the Director (see the *Par* section of the main configuration file). It sets the paths to store the acquired data and the resulting turbulence profiles, and the database parameters to store the final results such as seeing, free atmosphere seeing, and integrals of turbulence for the different altitudes.

```
{
   "sitepar": "par-pachon.json",
   "Server":{
     "socket": 20402, "wait": 30,
     "data path": "../data/",
     "profile_path": "./profile/"
   },
   "DB":{
     "active": 0,
     "host": "xxx", "user": "ringss", "password": "pw", "database":
     "pac",
     "profile_query": "INSERT IGNORE INTO `ringss` (time, star, zen,
     flux, see2, see, fsee, wind, tau0, theta0, totvar, erms, j0, j025,
     %s, %s, %s, %s, %s, %s, %s, %s, %s, %s)"
   }
}
   The instrument parameters file, e.g., par-pachon.json, contains the site- and
instrument-specific information:
   "telescope": { "D": 0.127, "eps": 0.53, "pixel": 1.41,
   "ringradpix":11.0, "ron":1.1},
   "site":{"name":"PACHONSM","lon":-70.7358,"lat":-30.2401},
   "profrest":{
     "mmax":20, "zgrid":[0,250,500,1000,2000,4000,8000,16000],
     "wav": [500,525,550,575,600,625,650,675,700,725,750],
     "sp":[0.65,0.774,0.755,0.73,0.704,0.673,0.617,0.568,0.495,
     0.427,0.3],
     "weightfile":"weights.json", "zmat":"zmat.json", "starcat":
     "starcat.json"
   },
   "Camera":{
     "library path": "/home/ringss/ASIStudio/lib/libASICamera2.so",
     "snapshot":{
      "exposure_time":10, "gain":200, "brightness":10,
      "bandwidth":80,
      "roi_x0":448, "roi_y0":28, "roi_width":1024, "roi_height":
      1024,
      "snapshot_fn": "snapshot.fits", "save_snapshot":0},
     "cube": {
      "number":2000, "max_attempts":10, "exposure_time":1,
      "gain":200,
      "brightness":10, "bandwidth":80,
      "roi_x0":936,"roi_y0":516,"roi_width":48,"roi_height":48,
```

```
"cube_fn":"cube.fits","save_cube":0,
"imavg_fn":"imavg.fits","save_imavg":0,"flux_thr":10000}
}
```

The *telescope* section specifies the aperture diameter (m), the central obscuration, the pixel size (arcsec), the ring radius (pixels), and the detector readout noise (electrons). These parameters are used to compute the relation between the statistical moments and turbulence, namely, the weighting functions (WFs).

The *site* section specifies the geographic coordinates needed for the calculation of the zenith distance.

The *profrest* section contains information required for data processing. The $m_{\rm max}=20$ is the maximum frequency of the angular coefficients in the moments file. The *zgrid* defines the number and heights of the layers in the reconstructed turbulence profile. The spectral response of the system (product of detector quantum efficiency and filter transmission) is defined by a list of wavelengths (in nanometer, preferably on a regular grid) and the response factors (with arbitrary normalization). The last parameters in this section are the names of the auxiliary files (in JSON format) used in the data processing, namely, the WFs, the aberration coefficients (optional), the so-called Z matrix (a fixed text file), and the star catalog.

The *Camera* section contains the information on the ZWO camera library file and the general parameters for snapshots and cubes.

5.2 Measurement Chain: Acquisition and Data Reduction

The software can be used in either automatic or supervised operation modes. In the supervised mode, ASI290mm.py can take snapshots to point and center the image. When the ring is centered, an image cube can be acquired and saved in a file. The turbulence profile and the full seeing are computed by processing the image cube.

In the automatic mode, the camera server ImageAcq_server.py imports ASI290mm.py and loads the configuration from imageacqsvr.cfg. The Director sends commands to the Camera software module server and waits for answers. The following Camera commands are available:

- INIT—set up the database connection, open files for saving the results.
- PARK—close the output files.
- RUN SNAPSHOT—take a wide 1024² pixel image (snapshot), determine the presence
 of a ring-like star image, and measure its center position. This procedure is based on
 corcent.py, where the wide-field snapshot image is correlated with a synthetic ring
 image to find the offset.
- RUN CUBE—take one data cube and process it using Moments. The statistical moments
 are written to the .stm file and are accumulated internally in the code. The cube and the
 average image can be optionally saved as fits files.
- RUN AVG—average the statistical moments accumulated from a given number of cubes and determine the turbulence parameters. Write the result to the text file and push it to the database.
- GET ERROR and GET STATUS—return these flags.
- SET STAR—write the star number and instrument parameters to the stm file.
- STOP—stop the camera.

Upon acquisition of an image cube, it is processed by cube2.py. Each ring image is accurately centered and multiplied by a set of fixed masks. The masks $C_m(r,\theta)$ and $S_m(r,\theta)$ are defined in polar coordinates as

$$C_m(r,\theta) = F(r)\cos(m\theta),\tag{2}$$

$$S_m(r,\theta) = F(r)\sin(m\theta),\tag{3}$$

where F(r) selects pixels with radii from $R_{pix} - \Delta r$ to $R_{pix} + \Delta r$ around the nominal ring radius R_{pix} with a half-width Δr 1.5 times larger than the expected diffraction width of the ring

(~3 pixels or 4.5"). The products of the bias-subtracted image and the masks are a series of coefficients c_m and s_m normalized by the flux c_0 . The variances of these coefficients and their covariances with a time lag of one frame are the statistical moments used for the OTP restoration (the cosine and sine variances are summed). The variances S_m are represented by a sum of k=8 layers at fixed distances z_k with turbulence integrals J_k

$$S_m = \sum_{k=1}^{8} W_m(z_k) J_k, \tag{4}$$

where $W_m(z)$ is the WF for angular frequency m.

In addition, the ring is divided into eight sectors, and the radii of these sectors are computed using suitable masks. Apart from the statistical moments, the .stm file records the average ring radii in the eight sectors and a few average coefficients, allowing us to measure quantitatively the low-order aberrations of the telescope (e.g., the coma is related to the average c_1 and s_1). The .stm file also records the star number in the bright stars catalog, the flux, image jitter, and some other parameters.

The operational algorithm consists of taking 10 consecutive data cubes and processing them individually; the results are written in the .stm file lines with a prefix m. In addition, the statistical moments are averaged and also written with a prefix M. The average moments are used for the OTP measurement, although the individual (unaveraged) moments can be used if needed, e.g., to check for consistency or to increase the temporal resolution. The OTP restoration from the average (rather than individual) moments reduces the impact of the measurement noise.

The WFs needed for the OTP measurement (Fig. 8) are computed by getweight5.py. Their dependence on the star color is accounted for by calculating the product of the instrument response and the black-body spectra with temperatures of 10,213 and 3938 K that correspond to the B-V colors of 0 and 1, respectively. The WFs are interpolated linearly in this range using the B-V color of the observed star. The WFs are computed for a fixed grid of 17 distances from 0 to 32 km with a logarithmic step of $\sqrt{2}$. The OTP is restored on a fixed grid of eight heights (which can be changed in the parameter file), and the WFs are interpolated on this grid while accounting for the zenith distance of the star. The resulting OTP thus always refers to observations at zenith.

Optionally, a list of Zernike numbers [zn] and their amplitudes [zrad] (in radians at the nominal wavelength specified by the parameters) can be given in the parameter file to correct the WFs for the aberrations. The aberstm.py stand-alone code reads the .stm file, computes the Zernike amplitudes from the mean coefficients, adds them to the aberration dictionary, and saves

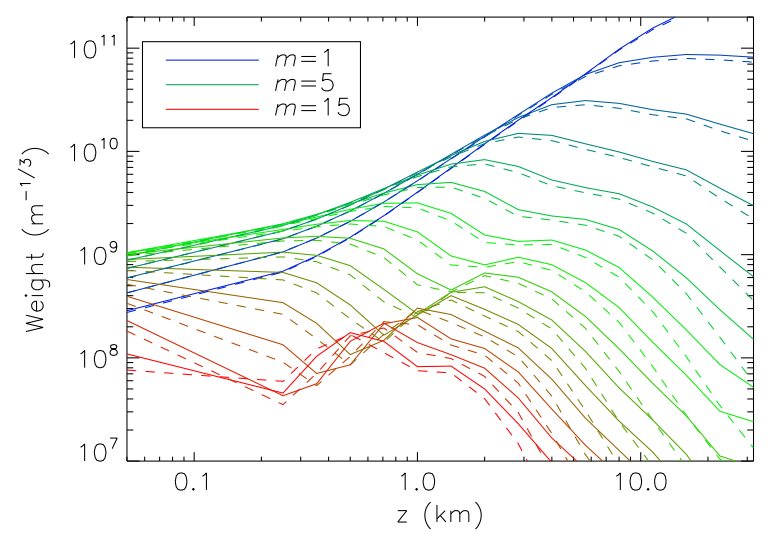


Fig. 8 Weighting functions used for the OTP restoration in RINGSS. Full lines plot the WFs for blue stars with B-V=0 and dashed lines for red stars with B-V=1. The z=0 layer is plotted at z=0.05 km.

Fig. 9 Example of the statistical moments and profile restoration. Panel (a) shows the variances and covariances as a function of the angular frequency m and the flat noise estimate (dotted line). After noise subtraction and correction to zero exposure, the moments from m=1 to m=15 [squares in panel (b)] are modeled by fitting an OTP (dashed line). In this case, most turbulence was concentrated in the two lowest layers.

it in the same parameter file. In this way, data from an aberrated telescope can be corrected *a posteriori* by re-calculating the WFs and repeating the OTP restoration.

For the OTP restoration, the variances and covariances at angular frequencies from 0 to $m_{\rm max}$ are retrieved from the .stm file. The estimated noise bias is computed using the noisepar parameters and the flux (converted from ADU to electrons according to the camera gain). The noise-subtracted variance is corrected for the finite exposure time bias and for the effect of saturated scintillation, as described in Ref. 14. The latter correction uses the so-called Z-matrix (fixed), which is available as a JSON file referenced in the parameters. The corrected variances S'_m at frequencies $m=1,\ldots 15$ (note the reduced maximum frequency) and the truncated matrix of weights $\mathbf{W}=W_m(z_k)$ are inputs to the restoration. The turbulence profile vector $\mathbf{J}=\{J_k\}$ must minimize the quadratic relative difference between measurements and their model, i.e.,

$$\sum_{m} ((\mathbf{WJ})_m - S'_m)^2 \to \min,\tag{5}$$

subject to the nonnegativity condition $J_k \ge 0$. The solution is found by the nonnegative least squares method. The signals S'_m vary by orders of magnitude, and the direct minimization of the difference between signals and model would try to accommodate the strongest (small-m) terms at the detriment of the weaker large-m signals. To remedy this, the lines of \mathbf{W} and the values of S'_m are weighted (multiplied) by 1/S (the uncorrected variance, always nonnegative). This modification effectively minimizes the sum of relative errors (Fig. 9). This approach has been originally developed and tested in the IDL version of the RINGSS code.

When the turbulence profile (vector \mathbf{J}) is found, the corresponding full seeing ϵ and the free-atmosphere seeing (0.5 km and above) are computed. The average variance of four sums of the radii of opposite pairs of the ring sectors provides an alternative measure of the seeing, ϵ_2 , analogous to a DIMM. As explained in Ref. 14, the coefficient relating this variance to the turbulence strength J depends on the distance, so the profile-weighted average of the pre-computed sector-motion WFs is used to compute ϵ_2 . Finally, the effective wind speed and the atmospheric time constant are calculated. The results are returned in the profile dictionary and pushed to the database for real-time access.

5.3 Robotic Control

The top-level diagram of software components and associated configuration files is given in Fig. 7. The components that manage mount, focuser, and dome are relatively simple. Each has its own small configuration file that defines the port address for communication and other device-specific parameters. For each component, a GUI interface is provided for debugging and testing. For example, the mount GUI allows full control for homing, slewing, and centering. However, in the robotic operation, these functions are accessed through the mount server.

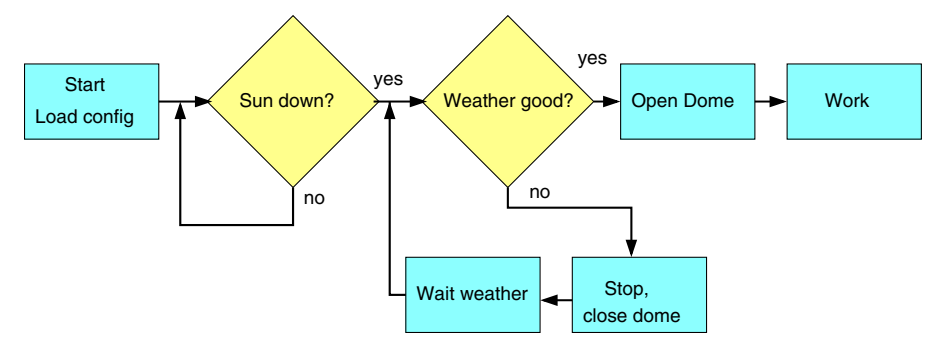


Fig. 10 Algorithm of monitoring observing conditions.

The program *Director* displays its own GUI and executes an endless loop in a thread. When the conditions for observations are good (sun below the horizon and weather within acceptable limits), it opens the dome (Fig. 10). Depending on the sidereal time, the star is selected from the pre-defined list by *Get_Object*. If it differs from the current star (None at the beginning), the procedure *Point* is activated. If the pointing fails (e.g., it is cloudy), the current object becomes invalid (None), the system waits for a certain time (specified in the configuration file), and repeats the pointing. Otherwise, the procedure cubes launch the loop of turbulence measurements. When the weather conditions are not adequate, *Stop* is executed (close the dome, park the mount), and the system waits for good weather. The observations stop in the morning when the sun is rising. This robotic sequence is executed in the AUTO mode; alternatively, pointing, measurement, and other actions can be commanded manually by buttons in the director GUI. The main procedures of the Director are explained below.

Pointing. The mount is commanded to slew to the R.A. and Decl. coordinates of the current object. Then, a snapshot image is taken using the CMOS camera in full-frame mode. The camera component returns the position of the star (ring) in pixels if it is found, and None if otherwise. The valid position is used to center the star ring image by executing the Guide procedure. The offsets in pixels are transformed to the mount correction commands using the rotation matrix M (M00, M01, M10, and M11 in the configuration file). If the duration of the correction exceeds a certain threshold (e.g., 5 s), the fast speed is used; otherwise, the slowest guiding speed is chosen. The sign of the correction in R.A. is inverted if necessary to account for the flips in the equatorial mode, and the R.A. (or AZ) correction is scaled (divided) by the cosine factor. Then, another snapshot is taken, and the centering is repeated a pre-defined number of times (usually a few cycles are needed) until the offsets become less than the tolerable threshold. If the pointing fails, the current object is set to none.

The *Cubes* procedure takes a pre-defined number of valid image cubes (e.g., 10), processes them, and computes the turbulence parameters. It sends the command RUN CUBE to the Camera software component and receives an answer telling whether the cube is valid or not. If a certain number of bad cubes are taken, the procedure exits, and a new pointing is forced. This happens, e.g., when the sky is cloudy. The last valid cube is used by the Director's procedures *Guide* and *Focus* to keep the star centered and the telescope focused. The corrections are applied only when the deviations exceed certain thresholds defined in the configuration. Average ring images obtained after cube processing are displayed in the *Director* GUI.

Focus takes the measured ring radius (in pixels) as input parameter and applies a focus correction if it differs from the nominal radius by more than the threshold. Corrections larger than 0.2 fraction of the nominal ring radius are not allowed (they likely originate from a wrongly processed cube).

To summarize, the operation can be roughly described by two loops: conditions monitoring (Fig. 10) and measurement (Fig. 11). A waiting period is defined for weather monitoring, so the dome is not re-opened too soon when conditions suddenly improve during the night. When the weather parameters are good but the sky is cloudy, the measurement loop tries to point to the star. If the pointing fails, a certain waiting period is imposed. The variable current_object defines whether the measurements can proceed or should be paused. The same variable manages changes in stars during the night.

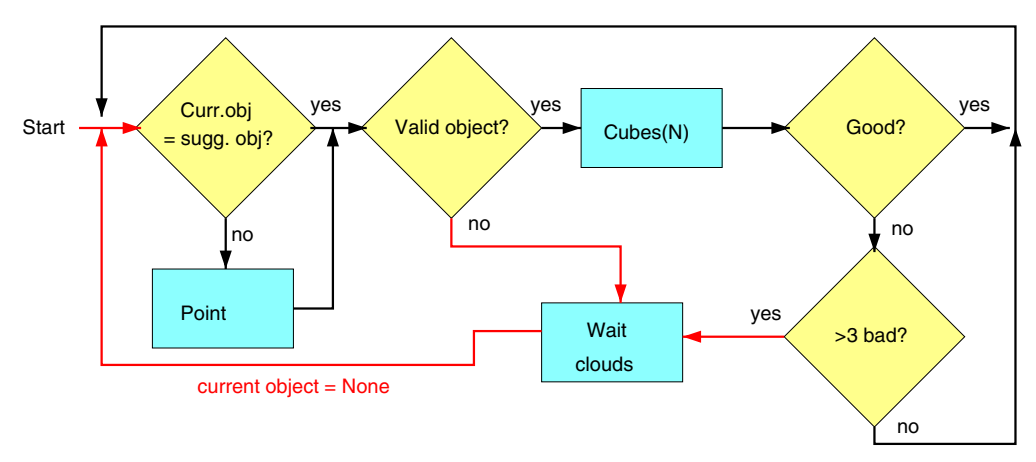


Fig. 11 Work algorithm. Red lines mark situations when the current object is None.

6 Sample Results

6.1 Comparison with MASS-DIMM at Cerro Tololo

The RINGSS turbulence profiler has been operating at Cerro Tololo in robotic mode since 2022 mid-November, installed in the cylindrical enclosure at a height of 6 m above the ground. A total of 46,129 turbulence measurements have been collected by February 15, 2023. The regular MASS-DIMM site monitor has been operational only for part of this period owing to problems with its mount and pointing; it stopped on January 8, 2023, and was back in service after February 15. Here, we compare the results of RINGSS and MASS-DIMM collected during this period and covering 58 nights of simultaneous operation. The DIMM data show a stable separation between the spots (mean 52.8 pixels, rms scatter 2.52 pixels) and large Strehl ratios (mean values of 0.80 and 0.78 for the left and right spots, respectively). Therefore, the DIMM data are accepted without any filtering. We matched 18,901 DIMM and 18,696 MASS measurements to the RINGSS data within 1 min in time. Below, we use the RINGSS seeing ϵ deduced from the OTP, not ϵ 2 from the differential sector motion.

Overall, the seeing measurements by DIMM and RINGSS agree very well. The mean and median seeing ratios RINGSS/DIMM are both 1.02. Figure 12 presents the comparison of the first 1000 time-matched samples and a density plot of all data. The formal linear regression is

$$\epsilon_{\text{RINGSS}} \approx -0.274 + 1.355 \epsilon_{\text{DIMM}}.$$
 (6)

One notes that when the seeing is poor, the RINGSS measures slightly larger values than the DIMM. Figure 12(a) illustrates how spikes of poor seeing are measured with a larger amplitude

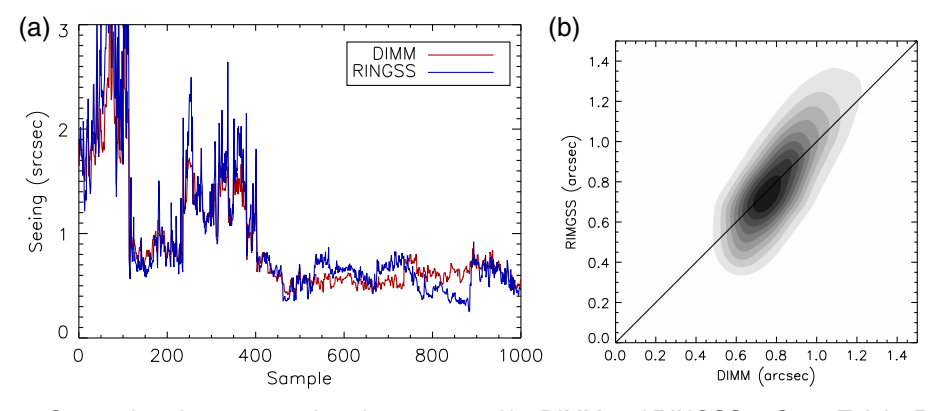


Fig. 12 Comparison between total seeing measured by DIMM and RINGSS at Cerro Tololo. Panel (a) shows seeing evolution versus time (the first 1000 of the 18,901 samples are plotted). Panel (b) is an *XY* comparison where the density of points corresponds to the gray shades.

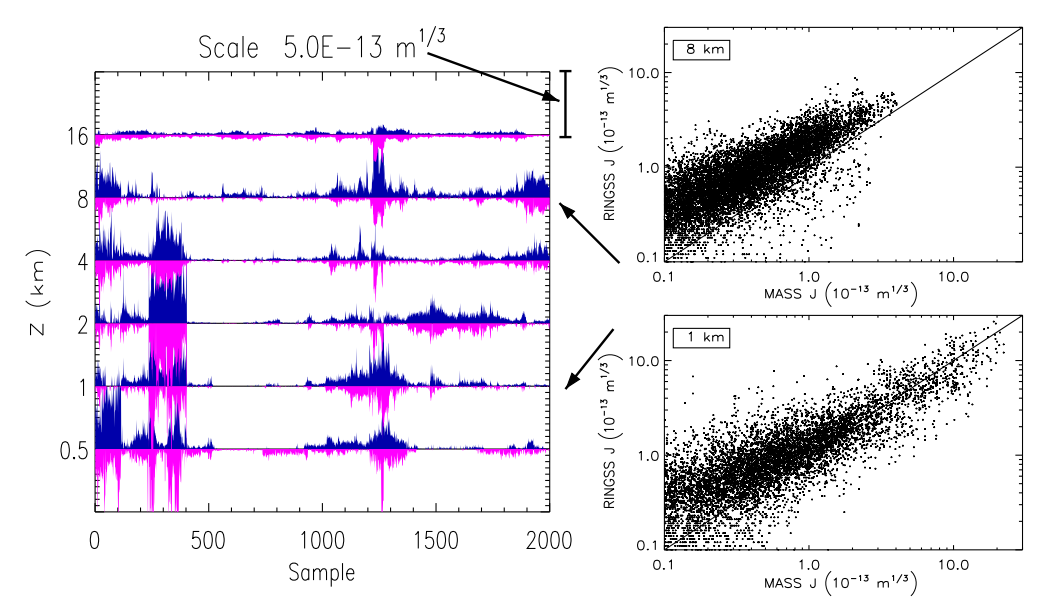


Fig. 13 Turbulence integrals J at Cerro Tololo in each layer versus sample number. The RINGSS data are up-facing blue bars, and MASS is plotted as down-facing magenta bars. The vertical interval between the lines corresponds to $J = 510^{-13}$ m^{1/3}. Two plots on the right compare the J values in the 1- and 8-km layers.

by RINGSS. These "overshoots" are associated with stronger scintillation, i.e., with high-altitude turbulent layers. The RINGSS software partially corrects for strong scintillation using a simulation-based prescription, as in MASS. However, the DIMM seeing is not corrected either for strong scintillation or for propagation (DIMM implicitly assumes turbulence concentrated near the ground), so under strong scintillation, DIMM is expected to under-shoot.

Figure 12(b) also evidences "local" disagreements between RINGSS and DIMM under very good (half arcsecond) seeing. The two instruments diverge in both directions, albeit mildly. The reason could be differences in the viewing directions (different stars) and local turbulence near each tower. The old DIMM is known to be affected by the local turbulence generated near the edge of the Tololo platform.²² Taken together, the combination of local turbulence under good seeing and under-shoots at poor seeing explains the slope of the formal linear regression.

The free-atmosphere seeing measured by RINGSS and MASS agrees very well: both the median and the mean ratio RINGSS/MASS is 1.11. The atmospheric time constant τ_0 is estimated by MASS very approximately and with a bias. When it is multiplied by 1.4, a good correlation with the more accurate RINGSS measurements of τ_0 is obtained. The turbulence profiles measured by RINGSS and MASS also agree quite well; see Fig. 13, where the first 2000 samples are plotted. A detailed layer-by-layer comparison (see figure 5 in the report available at Ref. 23) reveals minor systematic differences. For example, RINGSS puts more turbulence in the 8-km layer and less in the 16-km layer, compared with MASS.

6.2 Paranal Campaign

In February–March 2023, the RINGSS instrument worked for six nights at the Paranal observatory in a campaign organized by ESO. The results of this campaign are published by Griffiths et al., ²⁴ and only a brief summary is given here for completeness. RINGSS has been compared with a novel SHIMM profiler, ¹⁸ to the regular MASS-DIMM instrument, and to the Stereo-SCIDAR. All turbulence profilers have shown reasonably good mutual agreement. Most importantly, the high-resolution OTPs measured by the Stereo-SCIDAR, convolved with the vertical response of the RINGSS layers, agreed very well. In addition, the estimates of the atmospheric time constant τ_0 by both instruments were fully consistent.

The data of the Paranal campaign helped us to investigate the occasional discrepancy between the two alternative seeing estimates delivered by RINGSS, namely, the seeing ϵ derived

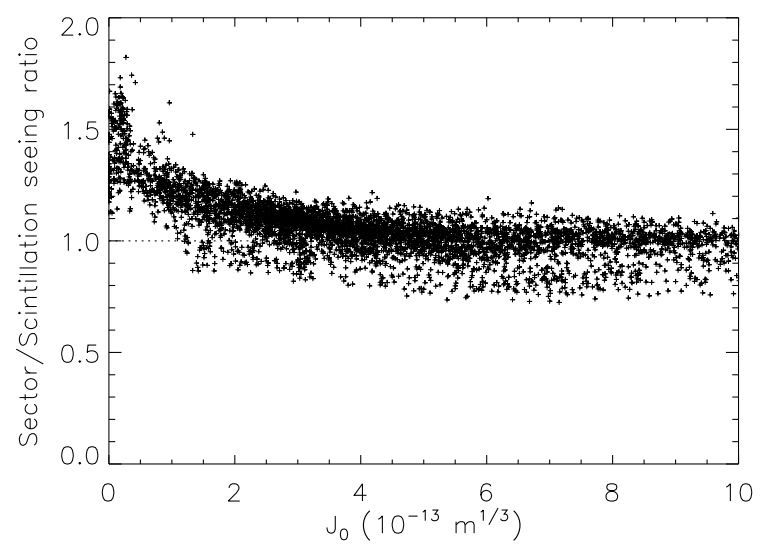


Fig. 14 Ratio of the two alternative seeing estimates ϵ_2 (from differential sector motion) and ϵ_2 (from scintillation) is plotted versus ground-layer turbulence integral J_0 . Data from the 2023 Paranal campaign, 5387 points.

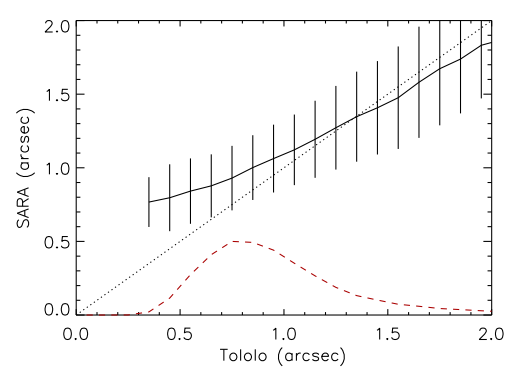
from the turbulence integral and based on the scintillation analysis, and the alternative seeing estimate ϵ_2 derived from the differential sector motion. Generally, these two estimates agree: the median ratio $r = \epsilon_2/\epsilon$ is 1.04 for the 5387 RINGSS measurements at Paranal. However, we noted that under very good seeing, ϵ_2 is systematically larger than ϵ . Their ratio shows a clear dependence on the turbulence intensity in the ground layer, J_0 (Fig. 14). In the absence of the ground-layer turbulence, the total seeing is dominated by the high layers. A larger than expected differential sector motion is attributable to the fact that the ring image is not perfectly focused in the radial direction, and fluctuations of the light amplitude at the pupil distort the ring shape, in analogy with a bias in a poorly focused DIMM. The scintillation-based seeing ϵ appears to be more robust, and the alternative estimate ϵ_2 is useful only for data quality control.

6.3 SARA-Tololo Campaign

This section illustrates the application of RINGSS as a site monitor. We investigated the seeing near the 60-cm SARA telescope installed at Cerro Tololo at several hundred meters from the main platform, at a lower elevation. We installed the second RINGSS instrument (same as used at Paranal) in a box-type enclosure (Sec. 4.3) on a 3-m high portable tower. The tower is assembled from three V-shaped elements, bolted together, and attached to three concrete pads in the ground. The data were collected in the period from November 11, 2023, to June 2, 2024. We retrieved the data from the regular RINGSS monitor at Tololo (Sec. 6.1) and analyzed the 76,214 simultaneous measurements, matched in time within 1 min, together with the weather data from Tololo. The time span of these data is almost half a year.

The full report on this campaign is available online. ²⁶ The representative results are shown in Fig. 15. The median seeing values at Tololo and SARA are 0.954" and 1.057", respectively. The difference between the sites is strongest under good seeing. It is produced by the stronger ground layer at SARA, expected for a site located below the main platform and the RINGSS installed in a lower 3-m tower. On the other hand, the free atmosphere seeing at both sites is identical, with a median value of 0.57", and the turbulence profiles in all layers above the ground measured by both instruments match well.

We explored how the difference in the near-ground turbulence integrals J_0 depends on the speed and direction of the wind at Tololo. As shown in Fig. 15(b), the ratio shows a clear dependence on the wind speed: it is close to one at both slow and fast wind and reaches a factor of two at a wind speed around 5 m/s. We also established that the ground-layer turbulence and the seeing at both sites are measurably better for the southern wind, compared with the dominant northern wind.



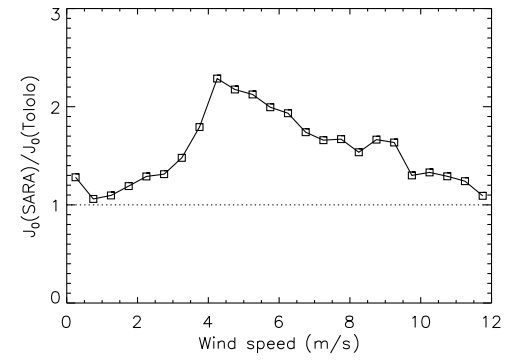


Fig. 15 (a) Seeing at SARA versus seeing at Tololo in bins of 0.1''. The solid line shows mean values, the bars are $\pm 1\sigma$ range, and the dotted line is a 1:1 relation. The red dashed curve shows the scaled histogram. (b) Ratio of the mean ground-layer turbulence integrals J_0 at both sites versus wind speed.

7 Summary and Outlook

We describe here a single-star turbulence profiler based on the RINGSS principle. Owing to the use of a compact 5-in. telescope and a compact mount, the whole instrument fits in a small volume. Therefore, instead of building an enclosure large enough to host persons (as was the case for the previous generation of site monitors), a compact enclosure is sufficient. Two concepts of such enclosures were developed and tested. A compact enclosure reduces both the wind buffeting and the locally generated turbulence.

The instrument can be made even smaller if a fork-type mount is used; then, the enclosure diameter could be reduced to \sim 0.4 m. An ideal solution would be an alt-alt mount surrounded by a small cylindrical or box enclosure. We have not found so far suitable commercial fork-type mounts, whereas the development of a custom mount and its control software is beyond our means.

Our experience indicates that the optical quality of the 5-in. Celestron telescopes is good and stable in time (no need to repeat the collimation). The RINGSS software measures the low-order aberrations, allowing stringent control of the optics. In principle, residual aberrations can be taken into account in the data processing. RINGSS measures several internal parameters characterizing the data quality, namely, the radius and width of the ring image, its position and jitter, and the rms error of fitting the OTP to the statistical moments. Comparison of two alternative seeing estimates, ϵ and ϵ_2 , serves as an additional quality check. A large pixel size of 1.5" and short 1-ms exposures make the instrument less sensitive to the wind-induced jitter, compared with classical DIMMs with ~ 0.6 " pixels and 5-ms exposure time.

So far, the main reasons for the failure of our RINGSS site monitors have been software errors of various kinds. For example, some astropy modules are self-updating, causing errors when the system has no internet connection. To increase the robustness of operation, we run the modules as Linux system services, and in the case of a module failure, it is restored automatically by the operating system.

Although the RINGSS instrument described here is assembled from commercial components, its duplication requires a certain expertise and effort. It would be desirable to procure a "turn-key" site monitor, complete with an enclosure, but such an option is not yet available. The demand for site monitors is too small to justify their serial production.

Disclosures

The authors declare there are no financial interests, commercial affiliations, or other potential conflicts of interest that have influenced the objectivity of this research or the writing of this paper.

Code and Data Availability

The IDL and Python versions of the code for turbulence measurements are available at Zenodo https://doi.org/10.5281/zenodo.14865456.

Acknowledgments

The development of RINGSS was supported by the National Science Foundation National Optical-Infrared Astronomy Research Laboratory (NSF's Noirlab). We thank Angel Otarola and Miska Le Louarn for the invitation to the Paranal campaign in 2023 and ESO's financial support.

References

- 1. V. I. Tatarskii, Wave Propagation in Turbulent Medium, McGraw-Hill (1961).
- 2. J. W. Goodman, Statistical Optics, Wiley-VCH (2000).
- 3. C. E. Coulman, J. Vernin, and A. Fuchs, "Optical seeing: mechanism of formation of thin turbulent laminae in the atmosphere," *Appl. Opt.* **34**, 5461 (1995).
- 4. F. Roddier, "The effects of atmospheric turbulence in optical astronomy," Prog. Opt. 19, 281–376 (1981).
- 5. A. Tokovinin, "The elusive nature of 'seeing'," Atmosphere 14, 1694 (2023).
- H. W. Shepherd et al., "Stereo-SCIDAR: optical turbulence profiling with high sensitivity using a modified SCIDAR instrument," *Mon. Not. R. Astron. Soc.* 437, 3568–3577 (2014).
- J. Osborn et al., "Turbulence velocity profiling for high sensitivity and vertical-resolution atmospheric characterization with Stereo-SCIDAR," Mon. Not. R. Astron. Soc. 464, 3998–4007 (2017).
- G. R. Ochs et al., "Refractive-turbulence profiles measured by one-dimensional spatial filtering of scintillations," *Appl. Opt.* 15, 2504–2510 (1976).
- J. L. Caccia, M. Azouit, and J. Vernin, "Wind and C(N)² profiling by single-star scintillation analysis," *Appl. Opt.* 26, 1288–1294 (1987).
- D. L. Fried, "Differential angle of arrival: theory, evaluation and measurement feasibility," *Radio Sci.* 10, 71–76 (1975).
- M. Sarazin and F. Roddier, "The ESO differential image motion monitor," Astron. Astrophys. 227, 294–300 (1990).
- V. Kornilov et al., "Combined MASS-DIMM instruments for atmospheric turbulence studies," Mon. Not. R. Astron. Soc. 382, 1268–1278 (2007).
- 13. M. Schöck et al., "Thirty meter telescope site testing I: overview," *Publ. Astron. Soc. Pac.* **121**, 384–395 (2009).
- A. Tokovinin, "Measurement of turbulence profile from defocused ring images," Mon. Not. R. Astron. Soc. 502, 794–808 (2021).
- 15. A. Guesalaga et al., "FASS: a turbulence profiler based on a fast, low-noise camera," *Mon. Not. R. Astron. Soc.* **501**, 3030–3045 (2021).
- H. Ogane et al., "Atmospheric turbulence profiling with multi-aperture scintillation of a Shack-Hartmann sensor," Mon. Not. R. Astron. Soc. 503, 5778-5788 (2021).
- 17. S. A. Potanin et al., "A facility for the study of atmospheric parameters based on the Shack–Hartmann sensor," *Astrophys. Bull.* 77, 214–221 (2022).
- 18. R. Griffiths et al., "Demonstrating 24-hour continuous vertical monitoring of atmospheric optical turbulence," *Opt. Express* **31**, 6730 (2023).
- 19. https://astronomy-imaging-camera.com/product/asi290mm.
- 20. https://www.zwoastro.com/product/asi462mm/.
- 21. https://www.ctio.noirlab.edu/~atokovin/ringss/.
- S. G. Els et al., "Four years of optical turbulence monitoring at the Cerro Tololo Inter-American Observatory (CTIO)," *Publ. Astron. Soc. Pac.* 121, 922–934 (2009).
- 23. https://www.ctio.noirlab.edu/~atokovin/ringss/report-feb2023.pdf.
- R. Griffiths et al., "A comparison of next-generation turbulence profiling instruments at Paranal," Mon. Not. R. Astron. Soc. 529, 320–330 (2024).
- A. Tokovinin and V. Kornilov, "Accurate seeing measurements with MASS and DIMM," Mon. Not. R. Astron. Soc. 381, 1179–1189 (2007).
- 26. https://www.ctio.noirlab.edu/~atokovin/ringss/SARA-report.pdf.

Edison Bustos is an electronics engineer with a master's in electrical engineering, specializing in software development for atmospheric turbulence instrumentation. With over 26 years of experience at AURA, Inc., he has played a key role in advancing observational technologies for astronomy. Based in Chile, he brings deep technical expertise and a passion for innovation to his work, contributing to critical infrastructure that supports world-class astronomical research across some of the most advanced observatories in the world.

Bustos, Tokovinin, and Rivera: Site monitor based on the RINGSS concept

Andrei Tokovinin obtained a PhD in astrophysics in 1980 at the Moscow State University and worked at the Sternberg Astronomical Institute before moving to CTIO (Chile) in 2001. His interests include astronomical instrumentation (adaptive optics, high-resolution spectroscopy, speckle interferometry), characterization of optical turbulence, and physics of multiple stars.

Rossano Rivera works in the NOIRLab-Chile since 1981 as a Mechanical Designer Draftsman. His areas of expertize are AutoCAD and Finite Element Analysis. He worked on the SOAR Telescope, Rubin Observatory, and numerous astronomical instruments.